



## RESEARCH LETTER

10.1002/2017GL073755

## Key Points:

- SWCCP is effective in suppressing multiple induced artificial events
- Applications of SWCCP to NECESSArray and USArray data reveal a negative event above the 410 km

## Correspondence to:

Z. Guan,  
guanphe9112@gmail.com

## Citation:

Guan, Z., and F. Niu (2017), An investigation on slowness-weighted CCP stacking and its application to receiver function imaging, *Geophys. Res. Lett.*, 44, doi:10.1002/2017GL073755.

Received 7 APR 2017

Accepted 7 JUN 2017

Accepted article online 9 JUN 2017

## An investigation on slowness-weighted CCP stacking and its application to receiver function imaging

Zhe Guan<sup>1,2</sup>  and Fenglin Niu<sup>1</sup>

<sup>1</sup>Department of Earth Science, William Marsh Rice University, Houston, Texas, USA, <sup>2</sup>Applied Physics Program, William Marsh Rice University, Houston, Texas, USA

**Abstract** Common conversion point (CCP) stacking of receiver functions is a widely used technique to image velocity discontinuities in the mantle. The CCP imaging technique assumes that receiver functions are composed solely of  $P$  to  $S$  conversions at velocity boundaries, whose depths can be mapped out through their arrival times. The multiple reflections at shallow boundaries with large velocity contrasts, such as the base of unconsolidated sediments and the Moho, can lead to artificial structures in the CCP images. We develop a refined CCP stacking method that uses relative slowness as a weighting factor to suppress the multiples (slowness-weighted CCP stacking, SWCCP). We conduct extensive numerical tests with synthetic data to seek the best weighting scheme and to verify the robustness of the images. We apply this technique to receiver function data of NECESSArray in China and the transportable array in western U.S. and find that most of the events in the depth range of 200–400 km shown in the regular CCP images are eliminated. The SWCCP images, on the other hand, reveal a clear negative event under some parts of the two arrays, indicating the presence of low velocity layer above the 410 km discontinuity, which was reported by previous studies.

### 1. Introduction

Mapping seismic velocity boundaries and scatterers in the mantle is of great importance in order to understand mantle composition and dynamics [e.g., *Shearer and Masters, 1992; Vidale and Benz, 1992; Wicks and Richards, 1993; Niu and Kawakatsu, 1995; Li et al., 1998; Shen et al., 1998; Simmons and Gurrola, 2000*]. Utilizing the  $P$ -to- $S$  and  $S$ -to- $P$  converted wavefield recorded by three-component seismic sensors plays a significant role in passive seismic imaging of the mantle [*Li et al., 2000; Niu, 2014*]. For example, source side  $S$ -to- $P$  converted waves have been used in determining the depths of the 410 km and 660 km discontinuities in the subduction zone in order to understand the nature of the two discontinuities and to constrain temperature in the transition zone [e.g., *Vidale and Benz, 1992; Wicks and Richards, 1993; Niu and Kawakatsu, 1995*]. Receiver side  $P$ -to- $S$  converted waves are widely used to map out depth variations of the Moho, mid-lithosphere discontinuity, and the lithosphere-asthenosphere boundary (LAB) beneath a seismic array.

Receiver functions are the Green's functions associated with structures beneath a receiver, which are obtained from three-component teleseismic records. More specifically, they are computed by a deconvolution of the radial/ $SV$  component by the vertical/ $P$  component [*Ammon, 1991*]. In a layered medium, a receiver function can be considered as the impulse response consisting of a direct  $P$  arrival and a series of conversions and reflections at boundaries below the station (Figure 1a). Because of the low amplitude of the conversion coefficients, stacking a large number of receiver functions is essential to obtain high-quality  $P$ -to- $S$  conversion data. The common conversion point stacking (CCP) [*Dueker and Sheehan, 1997; Gilbert et al., 2003; Niu et al., 2004, 2005; Schmandt et al., 2011, 2014; Tauzin et al., 2010, 2013*] is a widely used technique to gather and stack receiver function data to map mantle discontinuities and their lateral variations beneath a seismic array.

The CCP stacking method consists of two major steps. For an assumed discontinuity at depth,  $d$ , it first computes the arriving time of the  $S$  wave converted from  $P$  ( $Pd_s$ ) at the discontinuity, as well as its geographic location by ray tracing in a reference model. It then sums all the receiver functions that share similar conversion locations at the computed  $Pd_s$  time. The second step here actually assumes that receiver function data are solely composed of  $S$  waves converted from the incident  $P$  wave at different depths. In fact, the teleseismic impulse response contains both  $P$ -to- $S$  conversions and multiple reflections (Figure 1b). These multiples, which have relatively small moveout slope, would be inevitably stacked up to form artificial events that do not represent the true structures in the upper mantle. The multiple-related events occur in a wide depth

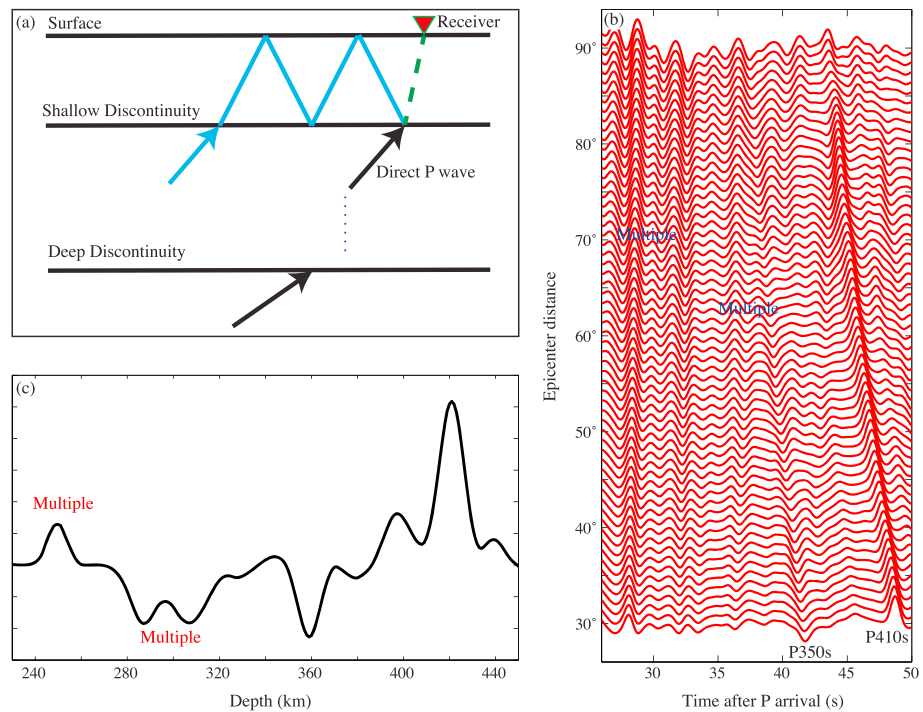


**Figure 1.** Illustration of how crustal multiples affect CCP imaging. (a) Schematic ray paths of a *P*-to-*S* conversion phase and a crustal multiple. (b) Multiples from the bottom of sediments and the Moho interfere with a hypothetical *P*-to-*S* conversion wave at 350 km. Note that the relative arrival times of the multiples increase with increasing epicentral distance, while the arrival time of P350s shows a decreasing trend. (c) A typical regular CCP stack, with prominent multiple-induced artificial events at shallow depths besides the two true conversion events at 350 and 410 km depths. To generate synthetic seismograms, we used a revised iasp91 model, which has a 3 km sediment layer with  $V_p = 3.08$  km/s,  $V_s = 1.54$  km/s, and  $\rho = 1.68$  g/cm<sup>3</sup>, underlain by a 37 km thick uniform crust with a  $V_p = 6.33$  km/s,  $V_s = 3.51$  km/s, and  $\rho = 2.91$  g/cm<sup>3</sup>.

range from approximately 100 to 400 km below the surface depending on the thickness of crust and the sediments (Figure 1c), which makes it difficult to interpret events in CCP images at these depths [Huang et al., 2010; Schmandt et al., 2012; Liu et al., 2015].

The presence of surface-related multiples in active seismic records, especially in marine seismic data, has been known for decades, and a variety of techniques have been developed to attenuate and eliminate these multiples [see Dragoset et al., 2010, and references therein]. In general, surface-related multiple elimination techniques can be divided into three categories: model driven, data driven, and something between. The model-driven approach employs wave equation-based forward modeling techniques to compute multiple reflections with an assumed Earth model, while the so-called data-driven methods predict multiples directly from the seismic records, which requires absolutely no knowledge of the subsurface. Once the multiple reflections are predicted from either a model or data, they are subsequently removed from the data by adaptive subtraction. The third approach utilizes the differences in the properties between the primary and multiples and employs adaptive filtering techniques to attenuate the multiples. Those techniques include common reflection point stacking [e.g., Mayne, 1962], Radon transform [Hampson, 1986], f-k filtering [e.g., Embree et al., 1963; Duncan and Beresford, 1994], etc.

Our approach to remove the multiple reflections falls in the third category. We notice the small and yet significant difference in (horizontal) slowness (i.e., ray parameter) between the *P*-to-*S* converted waves and the multiples. The relative slowness with respect to the direct *P* waves is negative for the conversions and positive for the multiples. Based on this difference, we design a weighting scheme to attenuate the multiples in performing the CCP stacking, which is referred to as slowness-weighted CCP stacking (SWCCP) hereafter. We conduct extensive numerical tests to investigate the effectiveness and robustness of different types of weighting schemes in terms of suppressing multiples and their smearing. By combining two weighting

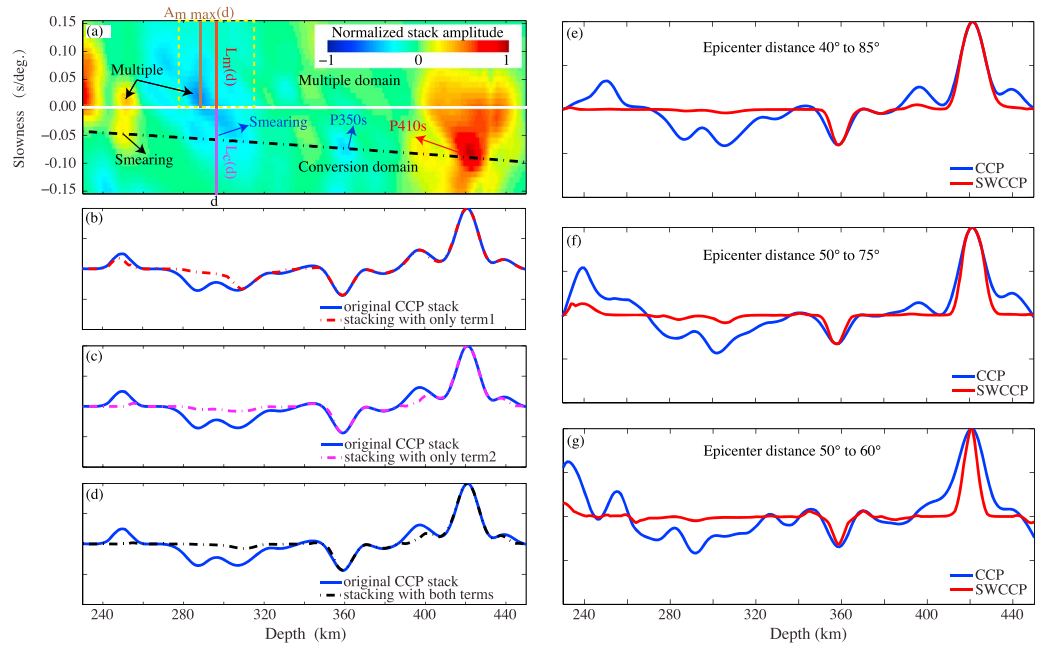


**Figure 2.** Effectiveness of two the slowness-based weighting schemes in suppressing multiples. (a) Depth domain tau- $p$  transform of the synthetic receiver functions shown in Figure 1b. The horizontal line at slowness 0.00 s/deg divides the tau- $p$  domain into the upper multiple and the lower conversion domain, respectively. The black dashed line in the conversion domain indicates the expected  $Pds$  slowness, which goes through the peak amplitude of the P350s and P410s. Multiples from the sediment base and the Moho generally peak in the upper multiple domain but smear severely to the conversion domain. (b, c) Weighted stacks using the first and second terms in equation (1) are plotted with the regular stack (blue). (d) The SWCCP stack, which combines both terms. Receiver functions in each depth cap are evenly distributed in the epicentral range of 30–90°. Comparisons of regular CCP with SWCCP stacks using receiver functions that are limited in epicentral distances: (e) 40° to 85°, (f) 50° to 75°, and (g) 50° to 60°. Even with a relatively narrow distance range of 10°, the SWCCP still possesses excellent ability in suppressing multiples.

schemes, we found that the SWCCP is very effective in removing multiple events from both synthetic and real data sets.

## 2. Method

Receiver functions in this study are computed from the  $SV$ - $P$  component pairs using the “water level” deconvolution technique [Clayton and Wiggins, 1976]. We set the water level to be 0.01, and the Gaussian function width to be 1.5, corresponding a corner frequency of 0.5 Hz.

Following the regular CCP stacking, for an assumed conversion depth,  $d$ , we first compute the  $Pds$  arrival time and geographic location of the conversion point for each receiver function. We then sort the receiver functions by their conversion points and gather all the receiver functions that share a common conversion location (cap). For the receiver functions gathered at each cap, we first align them by their epicentral distance and conduct the so-called slant stacking to estimate the relative slowness of a potential signal in the assumed  $Pds$  arrival time window. For an assumed slowness,  $p$ , we compute the linear moveout correction for each station by multiplying the slowness and relative epicentral distance ( $\Delta_i$ ) to the median epicentral distance ( $\Delta_0$ ), i.e.,  $p \times (\Delta_i - \Delta_0)$ . We then stack all the receiver functions after applying the moveout corrections. We vary the slowness between the range of  $\pm 0.15$  s/deg with an increment of 0.01 s/deg.

Figure 2a shows an example of stacked receiver functions in the depth range between 230 km and 450 km. The synthetic seismograms are evenly distributed in the distance range of 30°–90°, generated by a reflectivity method [Kennett and Kerry, 1979] with a revised iasp91 model, which has a 3 km sediment layer, a 40 km deep Moho, and a low-velocity layer (LVL) above the 410 km discontinuity. The LVL starts at the depth of 350 km with an  $S$  velocity drop of 0.1 km/s (2%) and extends to the 410 km. The vespagram clearly shows the two

conversions at the top of the LVL and the 410 km with a slightly negative slowness, together with at least three strong multiples that fall in the positive slowness domain (Figure 2a). Due to limitation in epicentral distance and the presence of side lobes, all the signals shown in the depth-slowness domain exhibit certain smearing along the slowness and depth axes (hereinafter referred to as slowness smearing and diagonal smearing, respectively), making it hard to utilize the slowness of the  $Pds$  arrival time window alone as the single parameter of a simple weighting scheme.

To take into account the slowness smearing, we first compare the observed slowness with the predicted  $Pds$  slowness and then compares the overall energy falls in the conversion or multiple domains. In detail, we first take a vertical slice (line) of the depth-slowness diagram along conversion depth,  $d$ , and search the slowness,  $p_o$ , at which the absolute stacking amplitude reaches its maximum. The uncertainty in slowness ( $\sigma_p$ ) is also estimated from the 95% confidence interval. More specifically, we fit the absolute stacking amplitude along the vertical line near  $p_o$  with a Gaussian function and compute its standard deviation  $\sigma$ .  $\sigma_p$  is then taken as  $2\sigma$ . The estimated  $\sigma_p$  is consistent with the uncertainty calculated with a bootstrap method [Efron and Tibshirani, 1986]. Next, we divide the vertical slice into the upper half and lower half, which are referred as multiple domain and conversion domain (Figure 2a), respectively, and compute the absolute average stacking amplitude in the conversion and multiple domains,  $|L|_c(d)$  and  $|L|_m(d)$ . Here we use  $L$  to indicate that the average is taken along a vertical line (e.g., purple and red lines in Figure 2a, respectively). To reduce the slowness smearing effect, we employ an exponential

function,  $e^{-\left\{\frac{(p_o - p_c)^2}{\sigma_p^2} + \frac{|L|_m}{|L|_c}\right\}}$ , to weight the regular CCP stack. Here  $p_c$  is the theoretical slowness of the  $Pds$ , which is expected to be negative. For a multiple signal, we expect a large difference between the observed and predicted slowness, as well as a high-amplitude ratio of  $|L|_m/|L|_c$ , leading to a small weight. On the other hand, the slowness difference and amplitude ratio are both small for a conversion phase, resulting in a weighting factor close to 1. An example on the weighting effect of this term is shown in Figure 2b.

For diagonal smearing related to side lobes, if there is a multiple reflection arriving within a time window 2 s before or after the  $Pds$ , then it can cause an amplitude hike in the conversion domain; we thus search the maximum absolute average amplitude in the expanded multiple domain and use its ratio with respect to the conversion average amplitude to reduce the diagonal smearing effect. In detail, we further extend the vertical slice to an  $\sim 40$  km wide window ( $d \pm 20$  km) centered at depth  $d$  (yellow dashed box in Figure 2a), which corresponds to a 4 s conversion time window, and is approximately twice as the dominant period (2 s) of the receiver function data. For each depth ( $x$ ) in the window, we first compute the absolute average amplitude of the multiple domain,  $|L|_m(x)$ , and select the maximum of  $|L|_m(x)$ , which is denoted as  $|A|_{m \max}$  (brown line in Figure 2a). In order to minimize the diagonal smearing, we use another exponential function of amplitude ratio  $|A|_{m \max}/|L|_c$  as the second weighting factor,  $w_2$ . The explicit format of  $w_2$  is shown in the following equation (1). If there is no interference with a multiple, the ratio is expected to be less than 1, then the weight is set to be 1. Figure 2c shows an example of the weighting with the second term. Figure 2d shows a comparison of a depth profile being processed with the regular CCP and SWCCP stacking methods; most of the multiples are effectively removed by the combination of the above two schemes. To summarize, we utilize two weighting factors to reduce the slowness and diagonal smearing of the multiples. The SWCCP stack amplitude is obtained by multiplying the regular CCP stack value with the two weighting factors:

$$\begin{aligned}
 \text{SWCCP}(x, y, d) &= \text{CCP}(x, y, d) \cdot e^{-\left\{\frac{(p_o(d) - p_c(d))^2}{\sigma_p^2(d)} + \frac{|L|_m(d)}{|L|_c(d)}\right\}} \cdot w_2, \quad \text{where} \\
 w_2 &= \begin{cases} e^{-\frac{|A|_{m \max}(d)}{|L|_c(d)}} & \text{if } |A|_{m \max}(d) \geq |L|_c(d) \\ 1 & \text{otherwise} \end{cases} \quad (1)
 \end{aligned}$$

Here  $x$  and  $y$  are geographic locations of the gathers and  $d$  is the conversion depth.

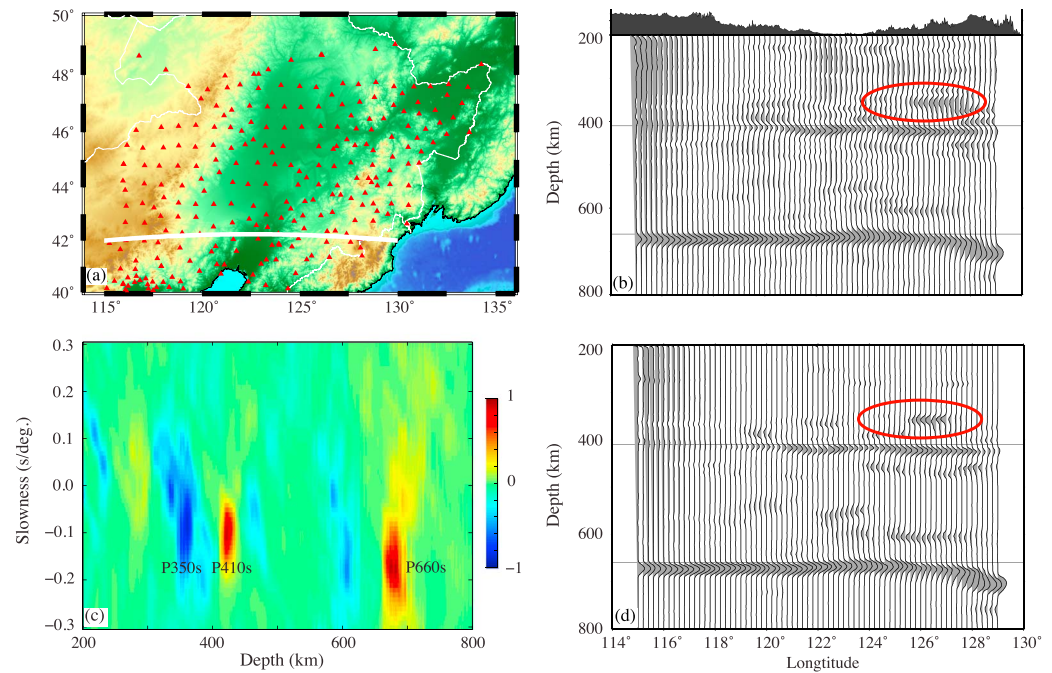


**Figure 3.** A comparison of CCP and SWCCP stacks of the NECESSArray data. (a) Topographic map of NE China. Red triangles denote the NECESSArray stations. The horizontal white line indicates the location of the E-W profile along the latitude of 42°N. (b, d) The regular CCP and SWCCP stacks along this profile. Note that most of the events above the 410 km shown in Figure 3b are absent in Figure 3d, indicating that they are multiple-related artificial events. (c) Results of the tau- $p$  transform using receiver functions gathered at various depth bins located at (126°E, 42°N). The ellipse in Figures 3b and 3d marks a prominent event with negative slowness located at ~350 km depth in Figure 3c, suggesting a plausible LVL atop the 410 km beneath this area.

### 3. Data Application

#### 3.1. NECESSArray

To illustrate the effectiveness of the SWCCP, we first applied it to a large receiver function data set recorded by the NECESSArray in northeast China [Tao *et al.*, 2014]. The NECESSArray consists of 127 temporary deployed between September of 2009 and August of 2011 and 128 permanent broadband stations of the China Earthquake Administration (Figure 3a). It provides a good coverage in the area of 116°–134°E and 40°–48°N where the Pacific plate subducted at the Japan reaches to the base of the upper mantle. Liu *et al.* [2015] conducted a CCP imaging study of the upper mantle beneath the array by using a total of 45,505 receiver functions. They found that the 660 km discontinuity exhibits significant depth variations beneath the study area. Meanwhile, there are many intermittent events above the 410 km discontinuity, with a potential LVL above the 410 km beneath some part of the array.

Figure 3b shows a latitudinal section of depth reflectivity profile (solid white line in Figure 3a) in the depth range of 200–800 km obtained from the regular CCP stacking. We employed a 3-D reference velocity model [Tao *et al.*, 2014; Tang *et al.*, 2014] to compute the  $P$ -to- $S$  conversion times. A circular cap with a radius of 1° is used here to gather receiver functions, and the depth increment is 1 km. Most caps have more than 600 receiver functions with epicentral distances widely distributed between 30° and 90°. Many intermittent structures can be found above the 410 km discontinuity. The SWCCP stacked result of the same section is shown in Figure 3d, which cleans up the shallow part of the image. Many events located above the 410 km discontinuity are effectively removed by the two weighting schemes. A negative event can be clearly seen at ~350 km in the eastern part of the section, which is consistent with the result based on  $ScS$  reverberation data [Revenaugh and Sipkin, 1994]. In Figure 3c, we also show the depth domain slant stacking at a grid (126°E, 42°N) where the 350 km negative signal is located in the conversion domain. The LVL was interpreted as a negatively buoyant silicate melt lying atop of the 410 km discontinuity.

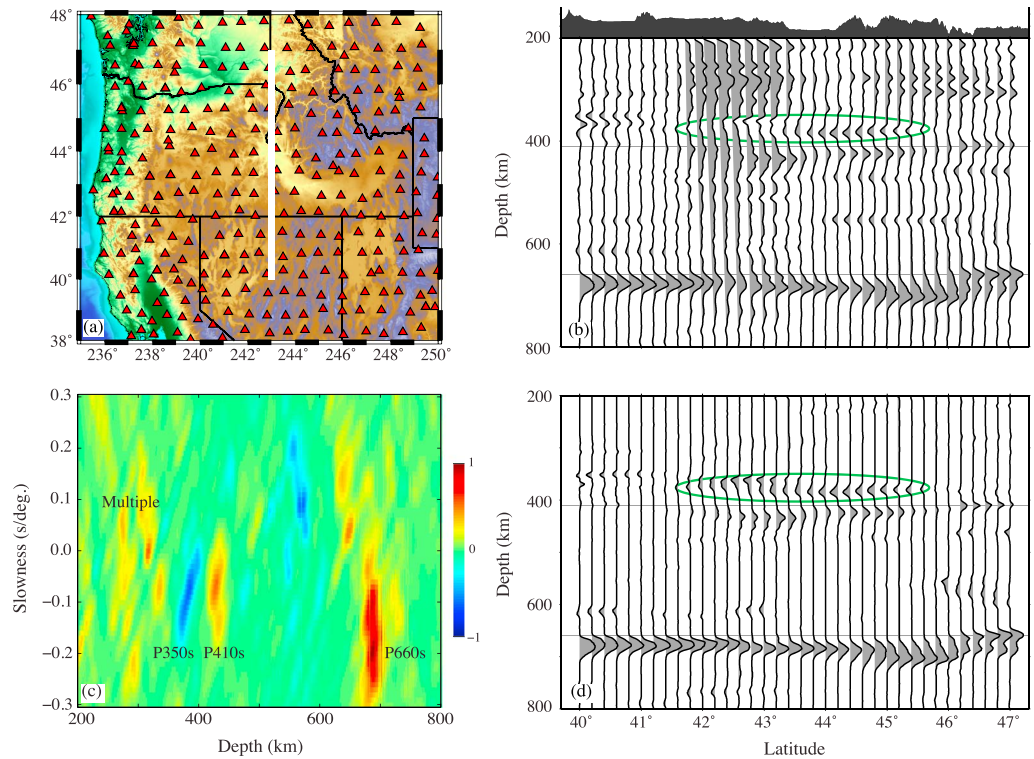


**Figure 4.** CCP and SWCCP stacking results of the USArray data. (a) Topographic map of the western U.S. with red triangles denoting stations of the Transportable Array. Vertical white line indicates the N-S profile along longitude of 117°W. (b, d) The regular CCP and SWCCP stacks along this profile. Note that most of the events above the 410 km shown in Figure 4b are absent in Figure 4d, indicating that they are multiple-related artificial events. (c) Results of the tau-p transform using receiver functions gathered at various depth bins located at (117°W, 44°N). The green ellipse in Figures 4b and 4d marks a plausible conversion event at ~350 km deep, which has been reported by several previous studies.

### 3.2. Transportable Array in Western U.S.

We also applied the SWCCP to receiver function data recorded by the transportable array (TA) stations in western U.S. to build a 3-D reflectivity volume [e.g., *Tauzin et al., 2013; Gao and Liu, 2014*] (Figure 4a). We selected a total of 18,404 receiver functions with high signal-to-noise ratio and applied both CCP and SWCCP stacking to the receiver function data.

Figure 4b shows the regular CCP stacking results along the 117° meridian west profile between 40° and 47°N (solid white line in Figure 4a). The iasp91 model [Kennett and Engdahl, 1991] is employed here as the reference model to compute the *Pds* conversion time. Again, a circular cap with a radius of 1° is used in gathering receiver functions, and the conversion depth range is 200–800 km with an increment of 1 km. The 660 km is clearly shown across all the section, which is ~680 km deep in the south, and gradually deepens toward the north. It reaches to a maximum depth of 700 km at ~45°N and shallows to 660 km at the northern end. The 410 km is obviously less evident. It is not clearly seen in the south section between 40.0° and 41.5°N and can be easily identified in the rest of the section (41.5°–47.0°N). The depth to the 410 km discontinuity appears to follow the depth trend of the 660 km, suggesting at least that part of the apparent depth variations observed here might be caused by unmodeled velocity anomalies in the upper mantle. The second root stacking likely leads to the small P410s/P660s amplitude ratio here. In addition to the 410 km and the 660 km, several events can be seen both in the transition zone and in the upper mantle above the 410 km. The slant stacking result at one grid point (117°W, 44°N) is shown in Figure 4c, which clearly shows that most of the events located in these two depth ranges have a positive slowness and therefore are likely caused by multiple reflections.

The SWCCP result is shown in Figure 4d; most of the events in the depths above the 350 km and in the mantle transition zone have disappeared from the image. There is a prominent negative event at the depth range of

360–395 km between 42° and 46°N, which is not attenuated by the filtering. Such a negative signal was also observed by several previous studies [e.g., Song *et al.*, 2004; Tauzin *et al.*, 2013] and was interpreted as the top boundary of a LVL atop the 410 km discontinuity, similar to the one observed beneath northeastern China as shown in the previous section. The negative signal has an amplitude comparable to that of the P410s, suggesting a significant drop of the *S* wave velocity in this layer, which was interpreted by partial melt. Hier-Majumder and Tauzin [2017] found that the distribution of the LVL spatially correlates with the presence of the subducted Farallon plate in the transition zone and suggested that the LVL has a composition slightly different from the rest of the upper mantle. They further infer that the release of volatiles from the subducted Farallon slab caused partial melt in the LVL, and the partially molten zone beneath western U.S. could act as a large regional reservoir of volatile species such as H or C.

#### 4. Discussion

It is well known that resolution of slowness in slant stacking is controlled by the distribution in epicentral distance of the data. The narrower the distance distribution, the harder it becomes to resolve the slowness in a tau-*p* diagram. The synthetic receiver functions used in the example of slant stacking shown in Figure 2a are distributed in an epicentral distance range from 30° to 90°, which leads to a good slowness resolution, making our weighting schemes efficient in attenuating multiples. Considering the uneven spatial distribution in global seismicity, it is possible that some of the array recordings could suffer from limited distribution in epicentral distance. To see how the SWCCP technique proposed here could be affected by the limited distribution in epicentral distance, we conducted numerical experiment with three sets of synthetic receiver functions, which have an epicenter distance range of 40°–85°, 50°–75°, and 50°–60°, respectively. The stacking results based on the regular CCP and the SWCCP methods of the three data sets are shown in Figures 2e, 2f, and 2g, respectively. In all the three cases, the SWCCP stacking performs better than the regular CCP in effectively attenuating multiples. In general, most temporal arrays can achieve a 10° distance range in teleseismic records with a 1 year to 2 year deployment, making it viable to apply the SWCCP technique to image the upper mantle.

It is worth noting that the negative slowness of the *P<sub>d</sub>s* phase is derived from a flat discontinuity. If the *P*-to-*S* conversion occurs at a dipping boundary, then horizontal slowness no longer remains as a constant, and the apparent slowness of the *P<sub>d</sub>s* phase thus can be positive depending on the dipping geometry and the *P* wave incident direction. For a plane *P* wave incident on a 30° dipping interface from the updip direction, the *P*-to-*S* converted wave can have a positive slowness of 0.01 s/deg. Therefore, if all the receiver functions are derived from earthquakes from a narrow back azimuthal range, the slowness-based filtering could weight down *P*-to-*S* conversions at highly dipping structures, leading to images of bias against dipping structures. In most cases, however, receiver functions at each CCP bin are gathered from earthquakes with various epicentral distances and back azimuths. We thus believe that the SWCCP is also feasible in imaging dipping structures, especially those with a moderate slope (<30°).

Lateral variations in crustal thickness can also affect the apparent slowness of the multiples, which may affect the weighting of the SWCCP. Receiver functions gathered in each bin are from stations located in circular area cocentered with the circular bin. The radius of the circular area increases with conversion depth and can reach to a few hundreds of kilometers for a targeted conversion depth of ~350 km. If the Moho underneath the whole circular area dips systematically to a direction, it might be possible to generate multiples with a negative slowness under some very special circumstance. However, when a large number of earthquakes with multiple epicentral distances and back azimuths are used, it is almost impossible to generate a systematic bias on slowness. This is well demonstrated by the above two examples.

In addition to the ~350 km negative conversion beneath some parts of NE China and western U.S. (Figures 3d and 4d), we also notice a negative signal at around 600 km depth beneath some parts of NE China (Figure 3d). The signal is featured by a negative slowness (Figure 3c), suggesting that it is another *P*-to-*S* conversion at ~600 km with a velocity decrease. Tauzin *et al.* [2013] also found a clear negatively polarized signal at ~590 km beneath southern part of the western U.S. We conducted SWCCP analysis with receiver functions recorded in the same area and confirmed that the signal has a negative slowness and is most likely a *P*-to-*S* conversion phase. Tauzin *et al.* [2013] interpreted the ~590 km negative discontinuities as a

boundary related either to an increased water content in the transition zone or an accumulated layer of oceanic material through the past 100 Myr or both.

So far we have demonstrated that the SWCCP technique is effective for structures deeper than 200 km due to the relatively large difference in slowness between the deep conversions and the shallow multiples. When *P*-to-*S* conversions occur at boundaries shallower than 200 km, such as the LAB and the midlithospheric discontinuity, the slowness difference becomes less and less significant, which is under the resolution ( $\sim 0.05$  s/deg) of the regular slant stacking technique employed here. Therefore, we do not expect that the SWCCP technique proposed here is effective to separate the LAB/midlithospheric discontinuity from crustal multiples without any modification. A recent study [Aharcaou and Levander, 2016] suggested that compressive sensing technique can significantly raise the slowness resolution in slant stacking; therefore, we plan to continue exploring the SWCCP technique with a focus on lithospheric structures.

## 5. Conclusions

We develop a slowness-based weighting scheme to suppress and eliminate multiple-related events in the receiver-function CCP images. The proposed filtering technique can deal efficiently with smearing caused by limited data coverage and side lobes. We applied the SWCCP to receiver functions computed from reflectivity synthetics and teleseismic records of two broadband seismic arrays in northeastern China and northwestern U.S. In general, the images derived from the SWCCP are much cleaner than those from the regular CCP stacking; many events in the depth range of 200–400 km are effectively removed by the filtering. The SWCCP images also reveal a prominent low-velocity layer right above the 410 km discontinuity beneath some parts of the two arrays.

## Acknowledgments

We would like to thank the IRIS data center for providing the NECESSArray and TA station data (<https://www.iris.edu/>) and Alan Levander and Steve Grand for helpful discussion. We also thank Kelly Liu and another anonymous reviewer for their constructive comments and suggestions, which significantly improved the quality of this paper. This work is supported by NSF EAR-1547228.

## References

- Aharcaou, M., and A. Levander (2016), A compressive sensing approach to the high-resolution linear Radon transform: Application on teleseismic wavefields, *Geophys. J. Int.*, *207*, 811–822, doi:10.1093/gji/ggw307.
- Ammon, C. J. (1991), The isolation of receiver effects from teleseismic P waveforms, *Bull. Seismol. Soc. Am.*, *81*(6), 2504–2510.
- Clayton, R. W., and R. A. Wiggins (1976), Source shape estimation and deconvolution of teleseismic bodywaves, *Geophys. J. Int.*, *47*(1), 151–177, doi:10.1111/j.1365-246X.1976.tb01267.x.
- Dragoset, B., E. Verschuur, I. Moore, and R. Bisley (2010), A perspective on 3D surface-related multiple elimination, *Geophysics*, *75*(5), 75A245–75A261, doi:10.1190/1.3475413.
- Dueker, K. G., and A. F. Sheehan (1997), Mantle discontinuity structure from midpoint stacks of converted P to S waves across the Yellowstone hotspot track, *J. Geophys. Res.*, *102*, 8313–8327, doi:10.1029/96JB03857.
- Duncan, G., and G. Beresford (1994), Slowness adaptive f-k filtering of prestack seismic data, *Geophysics*, *59*, 140–147.
- Efron, B., and R. Tibshirani (1986), Bootstrap methods for standard errors, confidence intervals, and other measures of statistical accuracy, *Stat. Sci.*, *1*, 54–75.
- Embree, P., J. P. Burg, and M. M. Backus (1963), Wide-band velocity filtering—The pie-slice process, *Geophysics*, *28*, 948–974.
- Gao, S. S., and K. H. Liu (2014), Mantle transition zone discontinuities beneath the contiguous United States, *J. Geophys. Res. Solid Earth*, *119*, 6452–6468, doi:10.1002/2014JB011253.
- Gilbert, H. J., A. F. Sheehan, K. G. Dueker, and P. Molnar (2003), Receiver functions in the western United States, with implications for upper mantle structure and dynamics, *J. Geophys. Res.*, *108*(B5), 2229, doi:10.1029/2001JB001194.
- Hampson, D. (1986), Inverse velocity stacking for multiple elimination, SEG Tech. Program Expanded Abstr. 1986, pp. 422–424, Soc. of Explor. Geophys., Houston, Tex.
- Hier-Majumder, S., and B. Tauzin (2017), Pervasive upper mantle melting beneath the western US, *Earth Planet. Sci. Lett.*, *463*, 25–35, doi:10.1016/j.epsl.2016.12.041.
- Huang, J., E. Vanacore, F. Niu, and A. Levander (2010), Mantle transition zone beneath the Caribbean-South American plate boundary and its tectonic implications, *Earth Planet. Sci. Lett.*, *289*(1–2), 105–111, doi:10.1016/j.epsl.2009.10.033.
- Kennett, B. L. N., and E. R. Engdahl (1991), Traveltimes for global earthquake location and phase identification, *Geophys. J. Int.*, *105*(2), 429–465.
- Kennett, B. L. N., and N. J. Kerry (1979), Seismic waves in a stratified half space, *Geophys. J. Int.*, *57*(3), 557–583, doi:10.1111/j.1365-246X.1979.tb06779.x.
- Li, A., K. M. Fischer, M. E. Wyssession, and T. J. Clarke (1998), Mantle discontinuities and temperature under the North American continental keel, *Nature*, *395*(6698), 160–163, doi:10.1038/25972.
- Li, X., R. Kind, K. Priestley, S. V. Sobolev, F. Tilmann, X. Yuan, and M. Weber (2000), Mapping the Hawaiian plume conduit with converted seismic waves, *Nature*, *405*(6789), 938–941, doi:10.1038/35016054.
- Liu, Z., F. Niu, Y. J. Chen, S. Grand, H. Kawakatsu, J. Ning, S. Tanaka, M. Obayashi, and J. Ni (2015), Receiver function images of the mantle transition zone beneath NE China: New constraints on intraplate volcanism, deep subduction and their potential link, *Earth Planet. Sci. Lett.*, *412*, 101–111, doi:10.1016/j.epsl.2014.12.019.
- Mayne, W. H. (1962), Common reflection point horizontal data stacking techniques, *Geophysics*, *27*(6), 927–938, doi:10.1190/1.1439118.
- Niu, F. (2014), Distinct compositional thin layers at mid-mantle depths beneath northeast China revealed by the USArray, *Earth Planet. Sci. Lett.*, *402*, 305–312, doi:10.1016/j.epsl.2013.02.015.
- Niu, F., and H. Kawakatsu (1995), Direct evidence for the undulation of the 660-km discontinuity beneath Tonga: Comparison of Japan and California array data, *Geophys. Res. Lett.*, *22*, 531–534, doi:10.1029/94GL03332.

- Niu, F., A. Levander, C. M. Cooper, C.-T. A. Lee, A. Lenardic, and D. E. James (2004), Seismic constraints on the depth and composition of the mantle keel beneath the Kaapvaal craton, *Earth Planet. Sci. Lett.*, 224(3–4), 337–346, doi:10.1016/j.epsl.2004.05.011.
- Niu, F., A. Levander, S. Ham, and M. Obayashi (2005), Mapping the subducting Pacific slab beneath southwest Japan with Hi-net receiver functions, *Earth Planet. Sci. Lett.*, 239(1–2), 9–17, doi:10.1016/j.epsl.2005.08.009.
- Revenaugh, J., and S. A. Sipkin (1994), Seismic evidence for silicate melt atop the 410-km mantle discontinuity, *Nature*, 369(6480), 474–476, doi:10.1038/369474a0.
- Schmandt, B., K. G. Dueker, S. M. Hansen, J. J. Jasbinsek, and Z. Zhang (2011), A sporadic low-velocity layer atop the western U.S. mantle transition zone and short-wavelength variations in transition zone discontinuities, *Geochem., Geophys., Geosyst.*, 12, Q08014, doi:10.1029/2011GC003668.
- Schmandt, B., K. Dueker, E. Humphreys, and S. Hansen (2012), Hot mantle upwelling across the 660 beneath Yellowstone, *Earth Planet. Sci. Lett.*, 331–332, 224–236, doi:10.1016/j.epsl.2012.03.025.
- Schmandt, B., S. D. Jacobsen, T. W. Becker, Z. Liu, and K. Dueker (2014), Dehydration melting at the top of the lower mantle, *Science*, 344(6189), 1265–1268.
- Shearer, P. M., and T. G. Masters (1992), Global mapping of topography on the 660 km discontinuity, *Nature*, 355, 791–796.
- Shen, Y., S. C. Solomon, I. T. Bjarnason, and C. J. Wolfe (1998), Seismic evidence for a lower-mantle origin of the Iceland plume, *Nature*, 395(6697), 62–65.
- Simmons, N. A., and H. Gurrola (2000), Multiple seismic discontinuities near the base of the transition zone in the Earth's mantle, *Nature*, 405(6786), 559–562, doi:10.1038/35014589.
- Song, T.-R. A., D. V. Helmberger, and S. P. Grand (2004), Low-velocity zone atop the 410-km seismic discontinuity in the northwestern United States, *Nature*, 427(6974), 530–533, doi:10.1038/nature02231.
- Tang, Y., M. Obayashi, F. Niu, S. P. Grand, Y. J. Chen, H. Kawakatsu, S. Tanaka, J. Ning, and J. F. Ni (2014), Changbaishan volcanism in northeast China linked to subduction-induced mantle upwelling, *Nat. Geosci.*, 7(6), 470–475, doi:10.1038/ngeo2166.
- Tao, K., F. Niu, J. Ning, Y. J. Chen, S. Grand, H. Kawakatsu, S. Tanaka, M. Obayashi, and J. Ni (2014), Crustal structure beneath NE China imaged by NECESSArray receiver function data, *Earth Planet. Sci. Lett.*, 398, 48–57, doi:10.1016/j.epsl.2014.04.043.
- Tauzin, B., E. Debayle, and G. Wittlinger (2010), Seismic evidence for a global low-velocity layer within the Earth's upper mantle, *Nat. Geosci.*, 3(10), 718–721, doi:10.1038/ngeo969.
- Tauzin, B., R. D. van der Hilst, G. Wittlinger, and Y. Ricard (2013), Multiple transition zone seismic discontinuities and low velocity layers below western United States, *J. Geophys. Res. Solid Earth*, 118, 2307–2322, doi:10.1002/jgrb.50182.
- Vidale, J. E., and H. M. Benz (1992), Upper-mantle seismic discontinuities and the thermal structure of subduction zones, *Nature*, 356, 678–683, doi:10.1038/356678a0.
- Wicks, C. W., Jr., and M. A. Richards (1993), A detailed map of the 660-kilometer discontinuity beneath the Izu-Bonin subduction zone, *Science*, 261, 1424–1427.